

# Dielectric constant of monolayer transition metal dichalcogenides across excitonic resonances

A. Thilagam\*

Information Technology, Engineering and Environment,  
University of South Australia, Australia 5095.

We analyze the dielectric-function spectra of low dimensional transition metal dichalcogenides (TMDCs) using a fully analytical model of the complex dielectric function that is applicable in fractional dimensional space. We extract the dimensionalities of the  $A$  and  $B$  excitons as well as their Lorentzian broadening widths by fitting the model to experimental data in the spectral range of photon energies (1.5 - 3 eV). Our results show the significant contribution of the lowest ground exciton state to the dielectric properties of exemplary monolayer materials ( $\text{MoS}_2$ ,  $\text{MoSe}_2$  and  $\text{WSe}_2$ ). The exciton dimensionality parametrizes the processes that underlie confinement and many-body Coulomb effects as well as substrate screening effects, which simplifies the analysis of electro-optical properties in low dimensional systems. This study highlights the potential of theoretical models as a valuable tool for interpreting the optical spectrum and in seeking an understanding of the correlated dynamics between the  $A$  and  $B$  excitons on the dielectric function of TMDCs.

## I. INTRODUCTION

The lattice dynamics[1–4] and dielectric properties [5–8] of low dimensional transition metal dichalcogenides,  $\text{MX}_2$  ( $M = \text{Mo}, \text{W}, \text{Nb}$  and  $X = \text{S}, \text{Se}$ ) are currently investigated with great interest for both theoretical studies [9–15, 15–20], and high-performance device applications [21–38]. Excitons are confined strongly in low dimensional transition metal dichalcogenides (TMDCs) and display notable spectral features with desirable photoluminescence properties [33, 39–47]. In Molybdenum disulfide ( $\text{MoS}_2$ ), a well known member of the TMDCs, there exist two pronounced peaks which are linked to the direct gap  $A$  and  $B$  excitons. These peaks arise due to the vertical transitions at the  $K$  point from a spin-orbit split valence band to a doubly degenerate conduction band with decrease in the number of lattice layers [48–53]. Ultrafast optical pump-probe spectroscopic measurements display enhanced transient absorption blue-shifts for the  $A$  and  $B$  excitons in the monolayer  $\text{MoS}_2$  due to repulsive inter-excitonic interactions, with non-trivial linewidth broadening effects [51].

The dielectric constant is an fundamental quantity that underpins experimental observables such as the refractive index and absorption coefficient [54–59] and provides valuable guidelines for the fabrication of optoelectronic and photonic devices. Due to reduced contributions from ionic and surface polarizabilities associated with one or cluster of atoms, the dielectric constant decreases with increase in the frequency of the electric field [54, 55]. Changes in the lattice structure that arise from frequency induced vibrations also contribute to an overall decrease of the polarization of the material. It is well known that the decreased dielectric screening and enhanced electron-electron correlation forces give rise to the high exciton binding energies noted in TMDCs [43, 48–50, 53, 60–62]. Excitons are shown to dominate the dielectric properties of ultra-thin  $\text{MoS}_2$  of less than 5-7 layers [63], with the dielectric function displaying an anomalous dependence on the layer number. Currently, there is lack of knowledge of the effect of the correlated dynamics between the  $A$  and  $B$  excitons [51] on the dielectric function of TMDCs.

A comprehensive understanding of the role of excitons in the vicinity of the optical region provides useful guidelines in exploiting the dielectric properties of monolayer transition metal dichalcogenides for novel applications such as solar cells [23, 64–67], single-layer transistors [68, 69] and light-emitting diodes [70–72]. These reasons form the main motivation for this study where we employ the fractional dimension space approach (FDSA) [73–83] to examine the dielectric properties of the monolayer  $\text{MoS}_2$  and related common TMDCs. The FDSA maps an anisotropic quantum quasi-particle in real space to an isotropic environment parameterized by a single quantity  $d$  ( $1 \leq d \leq 4$ ) [73–78] which may assume non-integer values. The parameter  $d$  is independent of the physical mechanisms that are linked to confinement effects in TMDCs, which simplifies the evaluation of electro-optical properties in low dimensional systems [59, 84]. The theoretical predictions using FDSA yields good agreement with experimental findings [75–77, 85], and provides qualitative insights that could be useful in the fabrication of devices. The FDSA enables understanding of the underlying quantum dynamical processes that control device operation, and provides valuable information on the cost effective fabrication of optical devices.

In this study, we compute the complex dielectric function of low dimensional transition metal dichalcogenides using a model of the exciton as a quasi-particle with arbitrary dimensions [59, 84]. In TMDCs, the exciton dimensionalities are known to vary between 1.7 and 2.5 [62] and may be quantified either by the ratio of the monolayer height to the exciton Bohr radius, or by the degree of confinement of the exciton within the monolayer plane. To this end, we analyze the contributions of the  $A$  and  $B$  excitons to the broadened complex dielectric constant based on the Kramers-Kronig relations. The calculations linked to these

---

\*thilaphys@gmail.com

relations are simplified as the fractional dimensionalities  $d_A$  and  $d_B$  incorporate the blue-shifted absorption shifts and broadening effects arising from the quantum correlated dynamics between the  $A$  and  $B$  excitons [51]. While the detailed analysis of the repulsive inter-excitonic interactions is beyond the scope of this study, we aim to extract approximate estimates of the broadening effects of the  $A$  and  $B$  excitons using the FDSA formalism in this study.

## II. THE DIELECTRIC CONSTANT OF LOW-DIMENSIONAL EXCITONS

### A. The dielectric constant in $d$ dimensions

The complex dielectric function  $\epsilon_\alpha(E)$  that is applicable in  $d$  dimensions reads as

$$\epsilon_d(E) = \frac{A_d R^{d/2-1}}{(E + i\gamma)^2} [g_d(\xi(E + i\gamma_b)) + g_d(\xi(-E - i\gamma_b)) - 2g_d(\xi(0))], \quad (1)$$

$$g_d(x) = \frac{2\pi\Gamma(\frac{d-1}{2} + x)}{\Gamma(\frac{d-1}{2})^2 \Gamma(1 - \frac{d-1}{2} + x) x^{d-2}} \left[ \cot \pi \left( \frac{d-1}{2} - x \right) - \cot \pi(d-1) \right], \quad (2)$$

$$\xi(x) = \left( \frac{R}{E_g - x} \right)^{\frac{1}{2}} \quad (3)$$

where  $\gamma$  is the finite width of the Lorentzian broadened transitions and  $E_g$  is the effective band gap of the bulk material that incorporates confinement effects. The symbol  $\Gamma(x)$  denotes the Euler gamma function,  $R$  is the effective Rydberg and  $A_d$  parametrizes the exciton oscillator strength. All bound and unbound states arising from Coulomb interactions are taken into account in Eq.1-3. Using Eq.1, we express the total dielectric function for the monolayer material via the Sellmeier equation and summing the contributions from the  $A$  and  $B$  excitons as

$$\epsilon_d^T(E) = C + \frac{a}{b - E^2} + \epsilon_{d_A}^A(E) + \epsilon_{d_B}^B(E + \delta) \quad (4)$$

where  $\epsilon_d^A(E)$  and  $\epsilon_d^B(E + \delta)$  are the dielectric function contributions due to the  $A$  and  $B$  excitons respectively. The term  $\delta$  quantifies the separation between the  $A$  and  $B$  excitonic peaks. The dimensions associated with the  $A$  ( $B$ ) exciton is denoted by  $d_A$  ( $d_B$ ). The finite width of the Lorentzian broadened transitions associated with the  $A$  ( $B$ ) exciton is denoted by  $\gamma_a$  ( $\gamma_b$ ).

Fig.1 a, b illustrates the decrease of the imaginary component ( $\epsilon_i$ ) of the  $A$  exciton and corresponding increase of  $\epsilon_i$  of the  $B$  exciton with increase of the effective dimensions of both excitons ( $A$  and  $B$ ). A decrease in the Lorentzian widths  $\gamma_a$  and  $\gamma_b$  results in sharper excitonic peaks as is to be expected. All other parameters used to generate Fig.1 a, b are listed below the figures. The strongly confined ground exciton state ( $d \approx 2$ ) contributes dominantly to the dielectric constant properties of the anisotropic material system as seen in Eqs.1 and 4. The contribution from the higher bound excitons states is significantly less as the oscillator strengths of the transitions ( $2s, 2p$ ) are substantially decreased in higher order exciton states.

Fig. 2 a, b highlights the links between the dimensionality of the  $A$  exciton, the dielectric constant as well as dimensionality of the  $B$  exciton. The dimension of the  $A$  exciton is fixed at  $d_A = 1.8$  in Fig.2 a, and at the higher  $d_A = 2.5$  in Fig.2 b. A gradual decrease in the imaginary component ( $\epsilon_i$ ) of the  $B$  exciton occurs with increase of its effective dimensionality. The results show that a lower exciton dimension  $d_A = 1.8$  is associated with a weakened contribution to the dielectric constant estimates by the  $B$  exciton. There is partial qualitative agreement of these results with experimental observations [51] of correlated interactions between the  $A$  and  $B$  excitons which are closely linked in momentum and energy space.

The complex spectral optical properties of low dimensional material systems are influenced by collision-induced excitonic linewidth broadening effects. The non-local quantum interaction between the  $A$  and  $B$  excitons is expected to influence the optical properties of highly confined material systems. A previous work has shown that the broadened  $B$  exciton linewidth is linked to a diminished peak spectral amplitude of the  $A$  exciton [51]. To this end, there is possibility that collision-induced excitonic linewidth broadening effects occurring at one exciton ( $A$  or  $B$ ) may influence the spectral amplitude of the adjacent exciton. The incorporation of non-local quantum interactions between the  $A$  and  $B$  excitons as carried out in an earlier work[86] is expected to introduce greater accuracy in the analysis of the mutually driven quantum correlated interactions between the  $A$  and  $B$  excitons.

### B. The $A$ and $B$ excitonic peaks in monolayer MoS<sub>2</sub>

The dielectric function of the monolayer MoS<sub>2</sub> displays three peaks that range from low to high energies and are labelled as  $A, B, C$  [52]. The  $A$  and  $B$  excitonic peaks arise from the electron-hole interaction between the spin-orbit split valence bands and the lowest conduction band at the  $K$  and  $K'$  points. The  $A$  ( $B$ ) exciton is formed from the spin-up (spin-down)

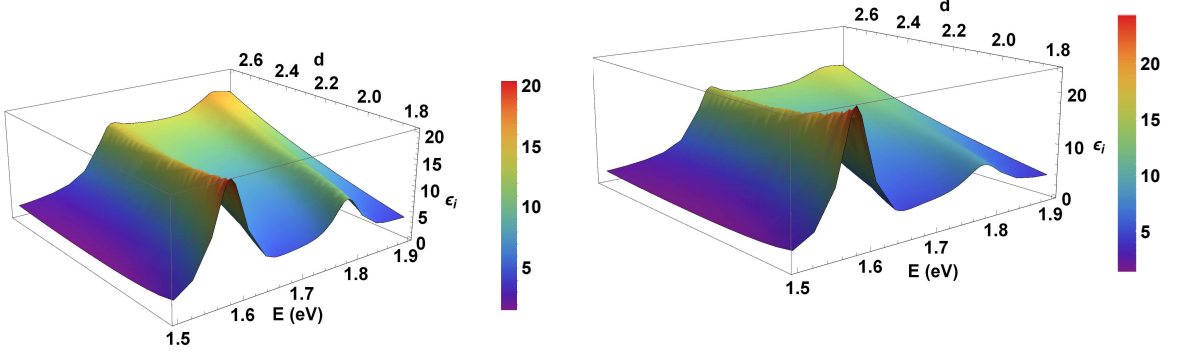


FIG. 1: (a) Imaginary component of the dielectric constant ( $\epsilon_i$ ) using Eq.4 as a function of energy  $E$  and the equal exciton dimensions  $d_A = d_B = d$ . We set the Lorentzian widths  $\gamma_a = 0.03$  eV,  $\gamma_b = 0.03$  eV, the effective Rydberg  $R = 0.015$  eV and take  $A_d R^{d_A/2-1} = 8$ ,  $A_d R^{d_B/2-1} = 4$ . We also set the effective band gap  $E_g = 1.68$  eV with  $\delta = 0.2$  eV. (b) Imaginary component of the dielectric constant using Eq.4 as a function of energy  $E$  and the equal exciton dimensionalities  $d_A = d_B = d$ . All other parameters used are the same as specified in (a) with the exception of  $\gamma_a = 0.025$  eV,  $\gamma_b = 0.04$  eV.

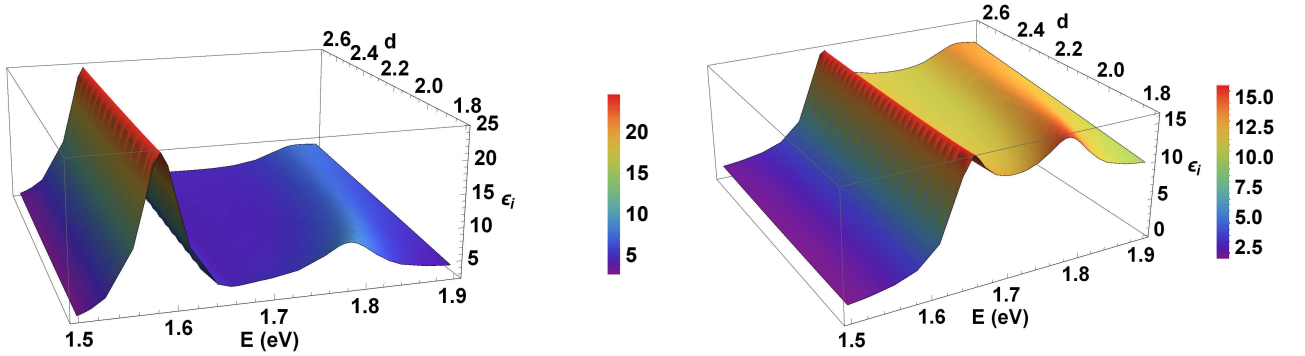


FIG. 2: (a) Imaginary component of the dielectric constant using Eq. 4 as a function of energy  $E$  and the exciton dimensions  $d_B = d$  with fixed  $d_A = 1.8$ . We set the Lorentzian widths  $\gamma_a = 0.025$  eV,  $\gamma_b = 0.04$  eV, and fix  $A_d R^{d_A/2-1} = 8$ ,  $A_d R^{d_B/2-1} = 4$ , the effective band gap  $E_g = 1.68$  eV and  $\delta = 0.2$  eV. (b) Imaginary component of the dielectric constant using Eq.4 as a function of energy  $E$  and the exciton dimensions  $d_B = d$  with fixed  $d_A = 2.5$ . All other parameters used are the same as specified in (a) above.

electrons in the conduction band (K-point of the BZ) and spin-down (spin-up) holes in the valence bands. The  $A$  and  $B$  excitons in general have almost similar behaviors, with any difference expected to arise from the position of holes in separate valence bands. The  $C$  peak is linked to electron-hole interaction between the valence band and the conduction band in the vicinity of the  $\Sigma$  and  $\Lambda$  points [53]. Ellipsometry optical techniques which allow the precise extraction of the dielectric function reveal the presence of the  $A$  and  $B$  exciton in the monolayer MoS<sub>2</sub> on SiO<sub>2</sub>/Si substrates at 1.88 eV and 2.02 eV respectively [87]. There exist three contributing factors to the dielectric constant in this region: 1) the lowest bound exciton, 2) all other higher bound exciton states, and 3) continuum contribution that incorporates a Sommerfeld factor due to Coulomb attraction. The weak higher bound exciton states tend to merge with increase in number of states, hence the contribution from the lowest bound exciton is considered separately from the rest of the higher bound states. With increase in the exciton binding energies at lower dimensions, the resonance energies of the monolayer dielectric function are shifted from the corresponding energies in the bulk material [5].

### C. Comparison of theoretical results with experimental data: monolayer MoS<sub>2</sub>

The complex in-plane dielectric functions of four monolayer TMDCs (MoS<sub>2</sub>, MoSe<sub>2</sub>, WS<sub>2</sub>, and WSe<sub>2</sub>) [5] have been derived using Kramers-Kronig constrained analysis of the reflectance spectra of the monolayers placed on fused silica substrates. Here we focus on the optical spectrum region (1.5 - 3 eV) [5] in the vicinity of the  $A$  and  $B$  excitonic peaks for the Molybdenum based monolayer materials: MoS<sub>2</sub> and MoSe<sub>2</sub>. We determine the dimensions of the  $A$  and  $B$  excitons ( $d_A$  and  $d_B$ ) as best-fit

parameters based on the experimental data of Li et. al. [5] and the *NonlinearModelFit* option in the Mathematica package. The nonlinear model for this procedure is constructed using the fractional dimensional space dielectric model of Eq. 4. Other than the dimensions  $d_A$  and  $d_B$ , we also determine  $A_1$  and  $A_2$  which are the respective amplitudes the  $A$  and  $B$  exciton, and the finite widths of excitonic transitions  $\gamma_a$  and  $\gamma_b$ . The band gap  $E_g$  and  $\delta$  which is the separation between the  $A$  and  $B$  excitonic peaks are taken as free parameters.

Fig. 3 illustrates the fitting of the experimental results of the imaginary component of the dielectric constant [5] for the monolayer MoS<sub>2</sub> material using the fractional dimensional dielectric model of Eq. 4. The best-fit parameters are extracted using the *NonlinearModelFit* function of Mathematica, with the effective Rydberg  $R$  fixed at a specific value. A range of values (40 to 60 meV) of  $R$  for the bulk MoS<sub>2</sub> [88] has been reported, and we thus fix  $R$  at two possible values of 45 meV and 55 meV. Using  $R=55$  meV, results of the fitting procedure give  $d_A = 2.0$ ,  $d_B = 1.95$ , effective band gap  $E_g = 2.11$  eV,  $\delta = 0.17$  eV, amplitudes  $A_1 = 2.27$  and  $A_2 = 8.65$  (blue line). The Lorentzian broadening widths are obtained as  $\gamma_a = 34$  meV ( $A$  exciton) and  $\gamma_b = 83$  meV ( $B$  exciton). Using  $R=45$  meV, results of the fitting procedure give  $d_A = 2.0$ ,  $d_B = 1.95$ , effective band gap  $E_g = 2.08$  eV,  $\delta = 0.17$  eV, amplitudes  $A_1 = 3.78$  and  $A_2 = 9.37$  (red line). The Lorentzian broadening widths using  $R=45$  meV are obtained as  $\gamma_a = 45$  meV ( $A$  exciton) and  $\gamma_b = 77$  meV ( $B$  exciton). The estimates for band gap  $E_g$  and the energy difference  $\delta$  between  $A$  and  $B$  excitonic peaks are in reasonable agreement with those obtained in an earlier work [49, 52]. The results here confirm that the ground exciton  $A$  and  $B$  states ( $d \approx 2$ ) contribute dominantly to the dielectric constant properties of the monolayer MoS<sub>2</sub> in the optical region (1.5 - 3 eV), with the exciton dimensionality playing a critical role in determining the dielectric properties of monolayer systems.

Using the hydrogenic binding energy relation

$$E_b = \frac{R}{\left(1 + \frac{d-3}{2}\right)^2} \quad (5)$$

we estimate the binding energy of the  $A$  exciton to be about 220 meV (using  $R=55$  meV) and 180 meV ( $R=45$  meV). The  $B$  exciton has binding energy of about 244 meV ( $R=55$  meV) and 200 meV ( $R=45$  meV), due to the higher hole mass of one of the spin-orbit split valence bands. These predicted results using Eq. 5 are substantially smaller than the binding energies ( $\approx 0.85$  eV) obtained in earlier works [49, 50, 52]. but in fair agreement with the well-converged first principle Bethe-Salpeter derived estimates (200 meV to 300 meV) by A. Molina-Sanchez et al. [44], and also with those of Berghäuser et al [89] who obtained binding energies of 455 (465 meV) for  $A$  ( $B$ ) excitons respectively. The scaling relation between band gap and exciton binding energy of 2D systems [90] implies typical exciton binding energies of around 400 to 500 meV for the monolayer MoS<sub>2</sub> on a silicon substrate. There is also some consistency of our results with the exciton binding energy of 0.3 eV computed using  $R=77$  meV in Ref.[20], and also with the photoluminescence excitation spectroscopy results of monolayer MoS<sub>2</sub> on fused silica which provided an exciton binding energy of 0.44 eV [91]. In the case of the MoS<sub>2</sub> monolayer in vacuum[89], larger binding energies of 860 and 870 meV were obtained for the  $A$ ,  $B$  excitons. Due to the screening effects induced by the substrate, the exciton binding energy is reduced which correlates with an increased exciton dimensionality.

For TMDC monolayers supported on SiO<sub>2</sub> substrates, the photoluminescence linewidth is generally larger than 10 meV at low temperatures. Based on the fitting results, the Lorentzian broadening widths of  $\gamma_a = 34$  meV (45 meV) ( $A$  exciton) and  $\gamma_b = 83$  meV (77 meV) ( $B$  exciton) at  $R=55$  meV (45 meV) are of the same order of the broadened width of 60 meV evaluated in an earlier work [92] for the monolayer MoS<sub>2</sub>. The broadening kinetics associated with the  $A$  ( $B$ ) exciton are known to arise from several sources: exciton-optical phonon [92–94], exciton-acoustic phonon interactions [92, 95], exciton-impurity scattering [96] and, inter-excitonic scattering processes [51, 97]. The larger broadened width of the  $B$  exciton can be attributed to its origin at the second valence band with availability of increased recombination pathways [92] compared to the  $A$  exciton. The differences in hole energy and population densities between the two distinct valence bands linked to the  $A$  and  $B$  excitons also account for broadening width differences in  $\gamma_a$  and  $\gamma_b$ .

#### D. Comparison of theoretical results with experimental data: monolayer MoSe<sub>2</sub>

In few-layer MoSe<sub>2</sub>, the indirect bandgap and direct bandgap are nearly degenerate unlike the MoS<sub>2</sub> system [98]. There exist subtle differences between the monolayers MoSe<sub>2</sub> and MoS<sub>2</sub> in terms of the reduced exciton mass, dielectric constants [99] and band gaps [98]. Fig. 4 illustrates the fitting of the experimental results of the imaginary component of the dielectric constant [5] for the monolayer MoSe<sub>2</sub> with the fractional dimensional dielectric model of Eq. 4. By fixing the effective Rydberg  $R$  at 50 meV, we get from the fitting procedure:  $d_A = 2.05$ ,  $d_B = 1.98$ , effective band gap  $E_g = 1.77$  eV,  $\delta = 0.24$  eV, amplitudes  $A_1 = 1.5$  and  $A_2 = 5.4$  and the Lorentzian broadening widths of  $\gamma_a = 29$  meV ( $A$  exciton) and  $\gamma_b = 82$  meV ( $B$  exciton). Using Eq. 5 and the exciton dimensions obtained here, the binding energy of the  $A$  exciton is evaluated as 181 meV and that of the  $B$  exciton as 208 meV. With the effective Rydberg  $R$  at 40 meV, we get the following results from the fitting procedure:  $d_A = 2.01$ ,  $d_B = 1.98$ , effective band gap  $E_g = 1.74$  eV,  $\delta = 0.22$  eV, amplitudes  $A_1 = 2.3$  and  $A_2 = 5.7$  and the Lorentzian broadening widths of  $\gamma_a = 40$  meV ( $A$  exciton) and  $\gamma_b = 70$  meV ( $B$  exciton). Using Eq. 5 and the exciton dimensions obtained for  $R=40$  meV,

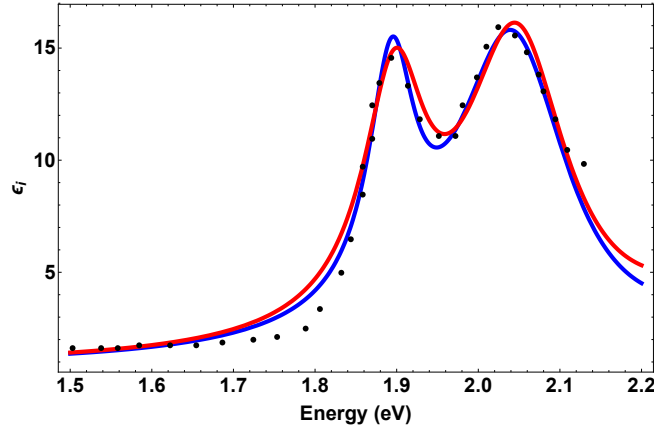


FIG. 3: Experimental results [5] of the imaginary component of the dielectric constant of the monolayer MoS<sub>2</sub> (dotted) fitted using the theoretical model ( $\epsilon_i$  in Eq.4). The best-fit parameters are determined via the *NonlinearModelFit* function of Mathematica, with the effective Rydberg  $R$  fixed at a specific value. The fitted parameters for the blue line are as:  $d_A = 2.0$ ,  $d_B = 1.95$ , effective band gap  $E_g = 2.11$  eV,  $\delta = 0.17$  eV, amplitudes  $A_1 = 2.27$  and  $A_2 = 8.65$  with  $R$  fixed at 55 meV. The Lorentzian broadening widths of  $\gamma_a = 34$  meV ( $A$  exciton) and  $\gamma_b = 83$  meV ( $B$  exciton).

The red line is obtained using  $R = 45$  meV and the fitted parameters are: the exciton dimensions  $d_A = 2.0$  and  $d_B = 1.95$ , effective band gap  $E_g = 2.08$  eV,  $\delta = 0.17$  eV, amplitudes  $A_1 = 3.78$  and  $A_2 = 9.37$  (red line). The Lorentzian broadening widths of  $\gamma_a = 45$  meV ( $A$  exciton) and  $\gamma_b = 77$  meV ( $B$  exciton).

the binding energy of the  $A$  exciton is evaluated as 160 meV and that of the  $B$  exciton as 167 meV. The Lorentzian broadening widths of the  $B$  exciton is larger than the  $A$  exciton for reasons mentioned in the earlier section for the monolayer MoS<sub>2</sub>.

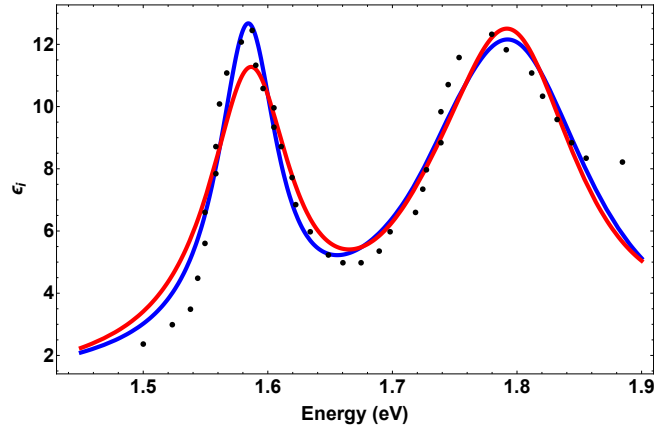


FIG. 4: Experimental results [5] of the imaginary component of the dielectric constant of the monolayer MoSe<sub>2</sub> (dotted) fitted using the theoretical model ( $\epsilon_i$  in Eq.4). The best-fit parameters derived using the *NonlinearModelFit* model (blue line) are as follows:  $d_A = 2.05$ ,  $d_B = 1.98$ , effective band gap  $E_g = 1.77$  eV,  $\delta = 0.24$  eV, amplitudes  $A_1 = 1.50$  and  $A_2 = 5.44$  with  $R$  fixed at 50 meV. The Lorentzian broadening widths of  $\gamma_a = 28$  meV ( $A$  exciton) and  $\gamma_b = 82$  meV ( $B$  exciton).

The red line is obtained using  $R = 40$  meV and the fitted parameters are: the exciton dimensions  $d_A = 2.0$  and  $d_B = 1.98$ , effective band gap  $E_g = 1.74$  eV,  $\delta = 0.22$  eV, amplitudes  $A_1 = 2.30$  and  $A_2 = 5.72$  (red line). The Lorentzian broadening widths of  $\gamma_a = 40$  meV ( $A$  exciton) and  $\gamma_b = 70$  meV ( $B$  exciton).

### E. Comparison of theoretical results with experimental data: monolayer WSe<sub>2</sub>

The exciton binding energy in monolayers of tungsten diselenide (WSe<sub>2</sub>) has been determined via optical techniques to be 0.37 eV with a band gap energy of 2.02 eV. Due to the strong spin-orbit coupling in WSe<sub>2</sub>, the energy separation between the  $A$  and  $B$  exciton is large (about 0.43 eV) [100]. Another study [101] revealed a much higher experimentally determined

exciton binding energy of 0.79 eV showing the large variations in binding energies that exists amongst different experimental and theoretical groups. Experimental determination of the exciton binding energy of monolayer WSe<sub>2</sub> was noted to be 240 meV on sapphire substrate while on gold the exciton binding decreased to 140 meV [7]. As expected, the enhanced screening by the metal substrate results in lower binding and a larger dimensionality for the exciton.

Fig. 5 illustrates the fitting of the experimental results of the imaginary component of the dielectric constant [5] for the monolayer WSe<sub>2</sub> with the fractional dimensional dielectric model (see Eq. 4). Instead of using fixed estimates for the effective Rydberg  $R$ , we allow the *NonlinearModelFit* function to yield appropriate values for  $R$ . We obtain two possible estimates:  $R=42$  meV and 52 meV and in both cases, we obtain slightly higher value for the dimensionality of the  $A$  exciton compared to the  $B$  exciton. The binding energies of the  $A$  ( $B$ ) exciton is about 231 meV (246 meV) for both values of the effective Rydberg. These binding energy estimates are comparable to that (240 meV) obtained on the insulator sapphire substrate by Part et. al. [7]. The electronic band gap of 1.89 eV for the monolayer WSe<sub>2</sub>/sapphire substrate configuration [7] agrees well with the estimate of  $E_g = 1.91$  eV obtained using the *NonlinearModelFit* model in Fig. 5.

The large energy separation between the  $A$  and  $B$  exciton state of  $\delta = 0.45$  eV derived here is consistent with an earlier result (0.43 eV) [100]. We note that the Lorentzian broadening widths of  $\gamma_b = 117$  meV ( $B$  exciton) is higher than the corresponding widths for the monolayer MoS<sub>2</sub> and MoSe<sub>2</sub> (see Table I). The large broadened width of the WSe<sub>2</sub> can be attributed to the enhanced recombination pathways at the location of the  $B$  exciton due to its large energy separation from the  $A$  exciton. It is likely that differences in hole population densities and exciton-phonon interactions between the two excitons further contribute to the wide variations seen in their Lorentzian broadening widths. Nevertheless further quantitative analysis is needed to identify the underlying factors that give rise to the wide difference in broadening widths between the  $A$  and  $B$  excitons. The theoretical fit around the region of the  $B$  exciton as shown in Fig. 5 also indicates that further refinement is needed in the fractional dimensional model used in this study. This will be considered in future works.

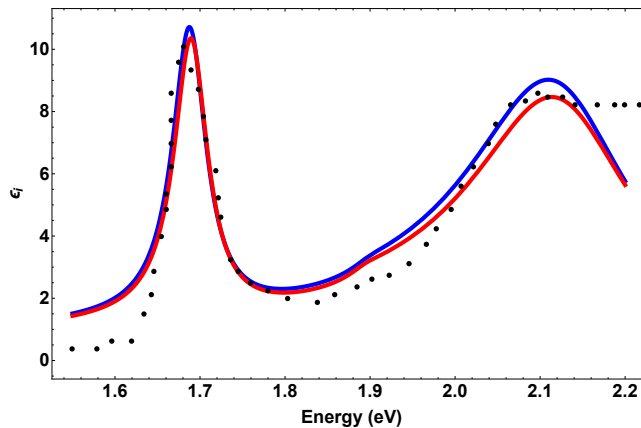


FIG. 5: Experimental results [5] of the imaginary component of the dielectric constant of the monolayer WSe<sub>2</sub> (dotted) fitted using the theoretical model ( $\epsilon_i$  in Eq.4). The best-fit parameters derived using the *NonlinearModelFit* model (see blue line) are as follows:  $d_A = 1.85$ ,  $d_B = 1.82$ , effective band gap  $E_g = 1.92$  eV,  $\delta = 0.45$  eV, amplitudes  $A_1 = 1.3$  and  $A_2 = 8.51$ , and the Rydberg  $R$  is obtained as 42 meV. The Lorentzian broadening widths of  $\gamma_a = 24$  meV ( $A$  exciton) and  $\gamma_b = 116$  meV ( $B$  exciton).

The red line is obtained using parameters derived from the fitting procedure:  $R=52$  meV, the exciton dimensions  $d_A = 1.95$  and  $d_B = 1.92$ , effective band gap  $E_g = 1.91$  eV,  $\delta = 0.45$  eV, amplitudes  $A_1 = 1.12$  and  $A_2 = 7.01$  (red line). The Lorentzian broadening widths of  $\gamma_a = 24$  meV ( $A$  exciton) and  $\gamma_b = 117$  meV ( $B$  exciton).

Table I shows a comparison of the various best-fit parameters using imaginary component of the dielectric constant of the monolayer MoS<sub>2</sub>, MoSe<sub>2</sub> and WSe<sub>2</sub>. The binding energies of the MoSe<sub>2</sub> based excitons are lower than the binding energies of the monolayer MoS<sub>2</sub>, in agreement with earlier results [52, 102]. The energy difference between the  $A$  and  $B$  transitions in the monolayer MoSe<sub>2</sub> is larger than that in MoS<sub>2</sub>, consistent with the result of Li et al [5] and Liu et al [103]. In comparison to the Molybdenum based monolayers, WSe<sub>2</sub> displays a larger Lorentzian broadening width,  $\gamma_b$ .

### III. CONCLUSION

In summary, we have examined the dielectric properties of low dimensional transition metal dichalcogenides using a fractional dimensional space model of the complex dielectric constant expression. Such a model simplifies the analysis of electro-optical properties in monolayer systems, and enables easy comparison between the different monolayer TMDCs. Our results show that the ground exciton state ( $d \approx 2$ ) contributes strongly to the dielectric constant properties of the material system. For

the monolayer materials ( $\text{MoS}_2$ ,  $\text{MoSe}_2$  and  $\text{WSe}_2$ ) examined here the oscillator strengths of the higher order exciton state transitions are substantially suppressed. For the purpose of rationalizing the excitonic features of different TMDCs, we extract the dimensionalities of the  $A$  and  $B$  excitons as well the broadening widths of excitonic transitions  $\gamma_a$  and  $\gamma_b$  using the theoretical model here and the experimental data of Li et. al. [5] based on monolayers ( $\text{MoS}_2$ ,  $\text{MoSe}_2$ ,  $\text{WSe}_2$ ) placed on fused silica substrates. We also extract the band gap  $E_g$  and the separation between the  $A$  and  $B$  excitonic peaks  $\delta$  using the fractional dimensional space model and a *NonlinearModelFit* function, with the effective Rydberg  $R$  fixed at a specific value in some cases.

There is good agreement between our theoretical predictions of the A-B splitting and the experimental results [5] for the monolayer TMDCs ( $\text{MoS}_2$ ,  $\text{MoSe}_2$ , and  $\text{WSe}_2$ ). The exciton binding energies agree reasonably well with exciton binding energy estimates obtained in earlier works [7, 20, 44, 89, 91]. The results in this study show that the  $B$  exciton has a marginally lower dimensionality than the  $A$  exciton in all the examined monolayer TMDCs. Moreover the non integer-dimensional occurrences of excitonic dimensionality presents as a reliable feature in computational modeling. The broadening width estimates of the  $A$  and  $B$  excitons ( $\gamma_a$ ,  $\gamma_b$ ) derived using the fractional dimensional model reveal a larger width for the  $B$  exciton which arises from differences in the environment of the two valence bands. The screening effects of the substrate influences the exciton dimensionality, and its binding energy. For instance, the enhanced screening by a metal substrate results in a larger exciton dimensionality compared to a monolayer placed on an insulator substrate. Thus exciton dimensionalities can be controlled via the dielectric environment presented by the substrate.

The results in this study show that a lower  $A$  exciton dimension is associated with a weakened contribution to the dielectric constant by the  $B$  exciton. This is in qualitative agreement with experimental observations [51] which show strong correlated inter-excitonic dynamics between the  $A$  and  $B$  excitons which are closely linked in momentum and energy space. Further understanding of the origin of the correlated dynamics between the  $A$  and  $B$  excitons and associated blue-shifted excitonic absorption could be useful for the design of quantum coupled optical devices. Lastly the fractional dimensional model of the complex dielectric function is useful for interpreting experimental data and making predictions for monolayer systems or properties that are not accessible via current experimental techniques.

TABLE I: Comparison of best-fit parameters obtained using the *NonlinearModelFit* function and the fractional dimensional space model of the complex dielectric constant for monolayer MoS<sub>2</sub>, MoSe<sub>2</sub> and WSe<sub>2</sub>. The effective Rydberg  $R$  is fixed for MoS<sub>2</sub> and MoSe<sub>2</sub> while it is extracted via the fitting procedure for WSe<sub>2</sub> (estimates with superscript).

System	$R$ (meV)	$d_A$	$d_B$	$\delta$ (meV)	$E_g$ (meV)	$\gamma_a$ (meV)	$\gamma_b$ (meV)	$A_1, A_2$	$A, B$ Exciton binding (meV)
MoS <sub>2</sub>	55	2.0	1.95	0.17	2.11	34	83	2.27, 8.65	220, 244 (cf 200 to 300 [44])
MoS <sub>2</sub>	45	2.0	1.95	0.17	2.08 (1.90, 2.05 [48])	45	77	3.78, 9.37	180, 200 (455, 465 [89])
MoSe <sub>2</sub>	50	2.05	1.98	0.24	1.77	28	82	1.50, 5.44	181, 208
MoSe <sub>2</sub>	40	2.0	1.98	0.22	1.74	40	70	2.30, 5.72	160, 167
WSe <sub>2</sub>	42*	1.85	1.82	0.45	1.92 (cf 1.89 [7])	24	116	1.3, 8.51	231, 246 (cf 240 [7])
WSe <sub>2</sub>	52*	1.95	1.92	0.45	1.91	24	117	1.12, 7.01	231, 246

- 
- [1] A. Molina-Sanchez and L. Wirtz, *Physical Review B* **84**, 155413 (2011).
- [2] W. Zhao, Z. Ghorannevis, K. K. Amara, J. R. Pang, M. Toh, X. Zhang, C. Kloc, P. H. Tan, and G. Eda, *Nanoscale* **5**, 9677 (2013).
- [3] Y. Cai, J. Lan, G. Zhang, and Y.-W. Zhang, *Physical Review B* **89**, 035438 (2014).
- [4] Q. Zheng, W. A. Saidi, Y. Xie, Z. Lan, O. V. Prezhdo, H. Petek, and J. Zhao, *Nano Letters* (2017).
- [5] Y. Li, A. Chernikov, X. Zhang, A. Rigosi, H. M. Hill, A. M. van der Zande, D. A. Chenet, E.-M. Shih, J. Hone, and T. F. Heinz, *Physical Review B* **90**, 205422 (2014).
- [6] A. Kumar and P. Ahluwalia, *Physica B: Condensed Matter* **407**, 4627 (2012).
- [7] S. Park, N. Mutz, T. Schultz, S. Blumstengel, A. Han, A. Aljarb, L.-J. Li, E. J. List-Kratochvil, P. Amsalem, and N. Koch, *2D Materials* **5**, 025003 (2018).
- [8] A. R. Klots, B. Weintrub, D. Prasai, D. Kidd, K. Varga, K. A. Velizhanin, and K. I. Bolotin, *Scientific reports* **8**, 768 (2018).
- [9] M. L. Trolle, T. G. Pedersen, and V. Véniard, *Scientific reports* **7** (2017).
- [10] T. C. Berkelbach, M. S. Hybertsen, and D. R. Reichman, *Physical Review B* **92**, 085413 (2015).
- [11] K. Kaasbjerg, K. S. Thygesen, and K. W. Jacobsen, *Physical Review B* **85**, 115317 (2012).
- [12] J. Zhou, W.-Y. Shan, W. Yao, and D. Xiao, *Physical review letters* **115**, 166803 (2015).
- [13] B. Mukherjee, F. Tseng, D. Gunlycke, K. K. Amara, G. Eda, and E. Simsek, *Optical Materials Express* **5**, 447 (2015).
- [14] T. Stroucken and S. W. Koch, *Journal of Physics: Condensed Matter* **27**, 345003 (2015).
- [15] M. Trushin, M. O. Goerbig, and W. Belzig, *Physical Review B* **94**, 041301 (2016).
- [16] B. Chakraborty, H. Matte, A. Sood, and C. Rao, *Journal of Raman Spectroscopy* **44**, 92 (2013).
- [17] A. Steinhoff, M. Florian, M. Rösner, M. Lorke, T. O. Wehling, C. Gies, and F. Jahnke, *arXiv preprint arXiv:1603.03633* (2016).
- [18] A. V. Kolobov and J. Tominaga, in *Two-Dimensional Transition-Metal Dichalcogenides* (Springer, 2016) pp. 321–363.
- [19] C. M. Chow, H. Yu, A. M. Jones, J. R. Schaibley, M. Koehler, D. G. Mandrus, R. Merlin, W. Yao, and X. Xu, *arXiv preprint arXiv:1701.02770* (2017).
- [20] D. B. Soh, C. Rogers, D. J. Gray, E. Chatterjee, and H. Mabuchi, *Physical Review B* **97**, 165111 (2018).
- [21] R. Woodward, R. Howe, T. Runcorn, G. Hu, F. Torrisi, E. Kelleher, and T. Hasan, *Optics express* **23**, 20051 (2015).
- [22] J. Z. Ou, A. F. Chrimes, Y. Wang, S.-y. Tang, M. S. Strano, and K. Kalantar-zadeh, *Nano letters* **14**, 857 (2014).
- [23] A. Pospischil, M. M. Furchi, and T. Mueller, *Nature nanotechnology* **9**, 257 (2014).
- [24] B. Radisavljevic, M. B. Whitwick, and A. Kis, *ACS nano* **5**, 9934 (2011).
- [25] S.-L. Li, K. Tsukagoshi, E. Orgiu, and P. Samorì, *Chemical Society Reviews* (2016).
- [26] D. Fan, H. Liu, L. Cheng, P. Jiang, J. Shi, and X. Tang, *Applied Physics Letters* **105**, 133113 (2014).
- [27] V. Perebeinos, *Nature nanotechnology* **10**, 485 (2015).
- [28] A. Beck, J. Bednorz, C. Gerber, C. Rossel, and D. Widmer, *Applied Physics Letters* **77**, 139 (2000).
- [29] D.-S. Tsai, K.-K. Liu, D.-H. Lien, M.-L. Tsai, C.-F. Kang, C.-A. Lin, L.-J. Li, and J.-H. He, *Acs Nano* **7**, 3905 (2013).
- [30] S. Wi, H. Kim, M. Chen, H. Nam, L. J. Guo, E. Meyhofer, and X. Liang, *ACS nano* **8**, 5270 (2014).
- [31] S. Xu, D. Li, and P. Wu, *Advanced Functional Materials* **25**, 1127 (2015).
- [32] S. Bertolazzi, D. Krasnozhan, and A. Kis, *ACS nano* **7**, 3246 (2013).
- [33] Q. Ji, Y. Zhang, T. Gao, Y. Zhang, D. Ma, M. Liu, Y. Chen, X. Qiao, P.-H. Tan, M. Kan, *et al.*, *Nano letters* **13**, 3870 (2013).
- [34] C.-H. Yu, M.-L. Fan, K.-C. Yu, V. P.-H. Hu, P. Su, and C.-T. Chuang, *IEEE Transactions on Electron Devices* **63**, 625 (2016).
- [35] D. Jariwala, A. R. Davoyan, J. Wong, and H. A. Atwater, *ACS Photonics* (2017).
- [36] M. Park, Y. J. Park, X. Chen, Y.-K. Park, M.-S. Kim, and J.-H. Ahn, *Advanced Materials* (2016).
- [37] S. Feng, C. Cong, N. Peimyoo, Y. Chen, J. Shang, C. Zou, B. Cao, L. Wu, J. Zhang, M. Eginligil, *et al.*, *Nano Research* , 1.
- [38] M. H. Woo, B. C. Jang, J. Choi, K. J. Lee, G. H. Shin, H. Seong, S. G. Im, and S.-Y. Choi, *Advanced Functional Materials* (2017).
- [39] A. Splendiani, L. Sun, Y. Zhang, T. Li, J. Kim, C.-Y. Chim, G. Galli, and F. Wang, *Nano letters* **10**, 1271 (2010).



- [40] G. Plechinger, F.-X. Schrettenbrunner, J. Eroms, D. Weiss, C. Schueller, and T. Korn, *physica status solidi (RRL)-Rapid Research Letters* **6**, 126 (2012).
- [41] Y. Zhu, J. Yang, S. Zhang, S. Mokhtar, J. Pei, X. Wang, and Y. Lu, *Nanotechnology* **27**, 135706 (2016).
- [42] G. Eda and S. A. Maier, *Acs Nano* **7**, 5660 (2013).
- [43] G. Berghäuser and E. Malic, arXiv preprint arXiv:1311.1045 (2013).
- [44] A. Molina-Sánchez, D. Sangalli, K. Hummer, A. Marini, and L. Wirtz, *Physical Review B* **88**, 045412 (2013).
- [45] C. Mai, A. Barrette, Y. Yu, Y. G. Semenov, K. W. Kim, L. Cao, and K. Gundogdu, *Nano letters* **14**, 202 (2013).
- [46] W. Gao, Y. H. Lee, R. Jiang, J. Wang, T. Liu, and X. Y. Ling, *Advanced Materials* **28**, 701 (2016).
- [47] S. Ghatak, A. N. Pal, and A. Ghosh, *Acs Nano* **5**, 7707 (2011).
- [48] K. F. Mak, C. Lee, J. Hone, J. Shan, and T. F. Heinz, *Physical Review Letters* **105**, 136805 (2010).
- [49] A. Ramasubramaniam, *Physical Review B* **86**, 115409 (2012).
- [50] T. Cheiwchanchamnangij and W. R. Lambrecht, *Physical Review B* **85**, 205302 (2012).
- [51] S. Sim, J. Park, J.-G. Song, C. In, Y.-S. Lee, H. Kim, and H. Choi, *Physical Review B* **88**, 075434 (2013).
- [52] H.-P. Komsa and A. V. Krasheninnikov, *Physical Review B* **86**, 241201 (2012).
- [53] D. Y. Qiu, H. Felipe, and S. G. Louie, *Physical review letters* **111**, 216805 (2013).
- [54] S. Wemple and M. DiDomenico Jr, *Physical Review B* **3**, 1338 (1971).
- [55] J. Hopfield, *Physical Review* **112**, 1555 (1958).
- [56] T. Takagahara, *Physical Review B* **47**, 4569 (1993).
- [57] S. Schmitt-Rink, D. Chemla, and D. Miller, *Advances in Physics* **38**, 89 (1989).
- [58] A. Yoffe, *Advances in Physics* **50**, 1 (2001).
- [59] C. Tanguy, P. Lefebvre, H. Mathieu, and R. Elliott, *Journal of applied physics* **82**, 798 (1997).
- [60] J. S. Ross, S. Wu, H. Yu, N. J. Ghimire, A. M. Jones, G. Aivazian, J. Yan, D. G. Mandrus, D. Xiao, W. Yao, *et al.*, *Nature communications* **4**, 1474 (2013).
- [61] A. M. Jones, H. Yu, N. J. Ghimire, S. Wu, G. Aivazian, J. S. Ross, B. Zhao, J. Yan, D. G. Mandrus, D. Xiao, *et al.*, *Nature nanotechnology* **8**, 634 (2013).
- [62] A. Thilagam, *Journal of Applied Physics* **116**, 053523 (2014).
- [63] Y. Yu, Y. Yu, Y. Cai, W. Li, A. Gurarlan, H. Peelaers, D. E. Aspnes, C. G. Van de Walle, N. V. Nguyen, Y.-W. Zhang, *et al.*, *Scientific reports* **5** (2015).
- [64] M.-L. Tsai, S.-H. Su, J.-K. Chang, D.-S. Tsai, C.-H. Chen, C.-I. Wu, L.-J. Li, L.-J. Chen, and J.-H. He, *ACS nano* **8**, 8317 (2014).
- [65] Y. Tsuboi, F. Wang, D. Kozawa, K. Funahashi, S. Mouri, Y. Miyachi, T. Takenobu, and K. Matsuda, *Nanoscale* **7**, 14476 (2015).
- [66] Y. Liu, W. Gao, and L. Hao, in *Novel Optical Materials and Applications* (Optical Society of America, 2016) pp. NoW1D–5.
- [67] A. Thilagam, *Journal of Mathematical Chemistry* **55**, 1 (2016).
- [68] D. Jariwala, V. K. Sangwan, D. J. Late, J. E. Johns, V. P. Dravid, T. J. Marks, L. J. Lauhon, and M. C. Hersam, *Applied Physics Letters* **102**, 173107 (2013).
- [69] Q. Zhang, W. Bao, A. Gong, T. Gong, D. Ma, J. Wan, J. Dai, J. N. Munday, J.-H. He, L. Hu, *et al.*, *Nanoscale* **8**, 14237 (2016).
- [70] C. S. Woodhead, J. Roberts, Y. J. Noori, Y. Cao, R. Bernardo-Gavito, P. Tovee, A. Kozikov, K. Novoselov, and R. J. Young, arXiv preprint arXiv:1607.05025 (2016).
- [71] P. J. Jeon, J. S. Kim, J. Y. Lim, Y. Cho, A. Pezeshki, H. S. Lee, S. Yu, S.-W. Min, and S. Im, *ACS applied materials & interfaces* **7**, 22333 (2015).
- [72] G. Clark, J. R. Schaibley, J. S. Ross, T. Taniguchi, K. Watanabe, J. R. Hendrickson, S. Mou, W. Yao, and X. Xu, *Nano letters* (2016).
- [73] F. H. Stillinger, *Journal of Mathematical Physics* **18**, 1224 (2008).
- [74] X.-F. He, *Physical Review B* **43**, 2063 (1991).
- [75] A. Matos-Abiague, L. Oliveira, and M. de Dios-Leyva, *Physical Review B* **58**, 4072 (1998).
- [76] P. Christol, P. Lefebvre, and H. Mathieu, *Journal of applied physics* **74**, 5626 (1993).
- [77] H. Mathieu, P. Lefebvre, and P. Christol, *PHYSICAL REVIEW B* **46** (1992).
- [78] P. Lefebvre, P. Christol, and H. Mathieu, *Physical Review B* **48**, 17308 (1993).
- [79] I.-K. Oh and J. Singh, *Physical Review B* **60**, 2528 (1999).
- [80] E. Reyes-Gómez, A. Matos-Abiague, C. Perdomo-Leiva, M. de Dios-Leyva, and L. Oliveira, *Physical Review B* **61**, 13104 (2000).
- [81] A. Thilagam, *Physical Review B* **56**, 4665 (1997).
- [82] A. Thilagam, *Physica B: Condensed Matter* **262**, 390 (1999).
- [83] M. Lohe and A. Thilagam, *Journal of Physics A: Mathematical and General* **38**, 461 (2004).
- [84] C. Tanguy, *Solid state communications* **98**, 65 (1996).
- [85] A. Thilagam, *Physical Review B* **56**, 9798 (1997).
- [86] A. Thilagam, *Journal of Physics A: Mathematical and Theoretical* **43**, 155301 (2010).
- [87] W. Li, A. G. Birdwell, M. Amani, R. A. Burke, X. Ling, Y.-H. Lee, X. Liang, L. Peng, C. A. Richter, J. Kong, *et al.*, *Physical Review B* **90**, 195434 (2014).
- [88] N. Saigal, V. Sugunakar, and S. Ghosh, *Applied Physics Letters* **108**, 132105 (2016).
- [89] G. Berghäuser and E. Malic, *Physical Review B* **89**, 125309 (2014).
- [90] Z. Jiang, Z. Liu, Y. Li, and W. Duan, *Physical Review Letters* **118**, 266401 (2017).
- [91] H. M. Hill, A. F. Rigosi, C. Roquelet, A. Chernikov, T. C. Berkelbach, D. R. Reichman, M. S. Hybertsen, L. E. Brus, and T. F. Heinz, *Nano letters* **15**, 2992 (2015).
- [92] A. Molina-Sánchez, M. Palumbo, A. Marini, and L. Wirtz, *Physical Review B* **93**, 155435 (2016).
- [93] P. Dey, J. Paul, Z. Wang, C. Stevens, C. Liu, A. Romero, J. Shan, D. Hilton, and D. Karaiskaj, *Physical review letters* **116**, 127402 (2016).

- [94] A. Thilagam, *Journal of Applied Physics* **120**, 124306 (2016).
- [95] A. Thilagam, *Journal of Applied Physics* **119**, 164306 (2016).
- [96] O. A. Ajayi, J. V. Ardelean, G. D. Shepard, J. Wang, A. Antony, T. Taniguchi, K. Watanabe, T. F. Heinz, S. Strauf, X. Zhu, *et al.*, *2D Materials* **4**, 031011 (2017).
- [97] F. Cadiz, E. Courtade, C. Robert, G. Wang, Y. Shen, H. Cai, T. Taniguchi, K. Watanabe, H. Carrere, D. Lagarde, *et al.*, *Physical Review X* **7**, 021026 (2017).
- [98] S. Tongay, J. Zhou, C. Ataca, K. Lo, T. S. Matthews, J. Li, J. C. Grossman, and J. Wu, *Nano letters* **12**, 5576 (2012).
- [99] I. Kylänpää and H.-P. Komsa, *Physical Review B* **92**, 205418 (2015).
- [100] K. He, N. Kumar, L. Zhao, Z. Wang, K. F. Mak, H. Zhao, and J. Shan, *Physical review letters* **113**, 026803 (2014).
- [101] A. Hanbicki, M. Currie, G. Kioseoglou, A. Friedman, and B. Jonker, *Solid State Communications* **203**, 16 (2015).
- [102] T. C. Berkelbach, M. S. Hybertsen, and D. R. Reichman, *Physical Review B* **88**, 045318 (2013).
- [103] G.-B. Liu, W.-Y. Shan, Y. Yao, W. Yao, and D. Xiao, *Physical Review B* **88**, 085433 (2013).